SCIENTIFIC REPORTS

OPEN

# Understanding of multi-level resistive switching mechanism in $GeO_x$ through redox reaction in $H_2O_2$/sarcosine prostate cancer biomarker detection

Received: 20 June 2017
Accepted: 29 August 2017
Published online: 11 September 2017

Subhranu Samanta[1], Sheikh Ziaur Rahaman[1,2], Anisha Roy[1], Surajit Jana[1], Somsubhra Chakrabarti[1], Rajeswar Panja[1], Sourav Roy[1], Mrinmoy Dutta[1], Sreekanth Ginnaram[1], Amit Prakash[1], Siddheswar Maikap[1,3], Hsin-Ming Cheng[4], Ling-Na Tsai[4], Jian-Tai Qiu[3,5] & Samit K. Ray[6,7]

**Formation-free multi-level resistive switching characteristics by using 10 nm-thick polycrystalline $GeO_x$ film in a simple W/$GeO_x$/W structure and understanding of switching mechanism through redox reaction in $H_2O_2$/sarcosine sensing (or changing $Ge^o$/$Ge^{4+}$ oxidation states under external bias) have been reported for the first time. Oxidation states of $Ge^0$/$Ge^{4+}$ are confirmed by both XPS and $H_2O_2$ sensing of $GeO_x$ membrane in electrolyte-insulator-semiconductor structure. Highly repeatable 1000 dc cycles and stable program/erase (P/E) endurance of $>10^6$ cycles at a small pulse width of 100 ns are achieved at a low operation current of 0.1 µA. The thickness of $GeO_x$ layer is found to be increased to 12.5 nm with the reduction of polycrystalline grain size of $<$7 nm after P/E of $10^6$ cycles, which is observed by high-resolution TEM. The switching mechanism is explored through redox reaction in $GeO_x$ membrane by sensing 1 nM $H_2O_2$, which is owing to the change of oxidation states from $Ge^0$ to $Ge^{4+}$ because of the enhanced $O^{2-}$ ions migration in memory device under external bias. In addition, sarcosine as a prostate cancer biomarker with low concentration of 50 pM to 10 µM is also detected.**

Recently, resistive switching random access memory (RRAM) has been specified as one of the most progressive next generation nonvolatile memories to replace 3D flash due to its simple metal-insulator-metal structure, complementary metal-oxide-semiconductor (CMOS) compatibility, low power consumption, better uniformity, strong data retention, long endurance, and easier fabrication with low cost[1–4]. The RRAM devices with several high-κ materials such as $Ta_2O_5$[5,6], $HfO_x$[7,8], $TiO_2$[9], $BaTiO_3$[10] have been reported by several groups. Along with these different oxides, the $GeO_x$ material has profound potential to execute resistive switching owing to its compatibility with back-end-of-line (BOEL) process in CMOS technology, capability of producing oxygen vacancy at low temperature[11], widely spanned dielectric constant values (k~12–15)[12], large band gap ($E_g$~4.3–5.9 eV)[13,14], and good thermal stability[15,16]. There are only few studies on $GeO_x$-based RRAM in literature. Applying plasma treatment, the current compliance (CC) is reduced to 600 µA in Ni/$GeO_x$/$TiO_y$/$N^+$ TaN RRAM stack[17]. Bipolar switching behaviors using $GeO_x$-based different memory structures have been demonstrated at CC of 3.5 µA[11]. A significant reduction of resistive switching variation has been achieved at a high CC of 50 mA in Au/Zr/$GeO_x$/YSZ/TiN structure[18]. In addition, multi-level cell (MLC) operation is also very important for high-density data

[1]Thin Film Nano Tech. Lab., Department of Electronics Engineering, Chang Gung University, 259 Wen-Hwa 1st Rd., Kwei-Shan, Tao-Yuan, 33302, Taiwan. [2]Electronics and Optoelectronics Research Laboratories, Industrial Technology Research Institute (ITRI), Hsinchu, 310, Taiwan. [3]Division of Gyn-Oncology, Department of Obs/Gyn, Chang Gung Memorial Hospital (CGMH), Tao-Yuan, 33302, Taiwan. [4]Material and Chemical Research Laboratories, Industrial Technology Research Institute, Hsinchu, 310, Taiwan. [5]Department of Biomedical Sciences, School of Medicine, Chang Gung University (CGU), Tao-Yuan, 33302, Taiwan. [6]Department of Physics, Indian Institute of Technology, Kharagpur, 721302, India. [7]S. N. Bose National Centre for Basic Sciences, J D Block, Sector III, Salt Lake City, Kolkata, 106, India. Correspondence and requests for materials should be addressed to S.M. (email: sidhu@mail.cgu.edu.tw)

storage RRAM application. There are few reports on MLC operation by using $Pt/Ta_2O_5/TiN$[19], $Ta/TaO_x/Pt$[20], $TiN/HfO_x/Pt$[21], $Pt/HfO_2/TiO_2/ITO$[22] and $TiN/Ti/TiO_{2-x}/Pt$ $NC/TiO_{2-x}/Au$[23] structures. Further, the switching mechanism is not explored clearly. Apart from those different electrode materials, tungsten (W) as a electrode material is also very useful in metal-insulator-metal (MIM) structure because of its CMOS compatibility, easier to complete RESET process, high electron emissivity, thermally and chemically stable[24]. A simple formation-free $W/GeO_x/W$ RRAM device with low operation current of 0.1–100 µA and proper switching mechanism evaluation through $H_2O_2$ sensing at a low concentration of 1 nM by oxidation state changing from Ge ($Ge^0$ to $Ge^{4+}$) in electrolyte-insulator-semiconductor (EIS) structure has not been reported yet. Further, prostate cancer is most common male malignancy in the western world and accountable for second most common male cancer related deaths[25]. According to Koutros *et al*., sarcosine is one of the biomarkers of prostate cancer[26]. Therefore, sarcosine[27] has been also detected by using electrolyte-insulator-semiconductor (EIS) structure in this study, which has been not reported yet.

In this study, we have manifested formation-free MLC resistive switching having the range of CCs from 0.1 µA to 100 µA and modulation of negative voltages by using $GeO_x$ material in a simple $W/GeO_x/W$ structure and the switching mechanism through redox reaction in $H_2O_2$ sensing has been explored owing to oxidation states changing of $Ge^0/Ge^{4+}$ under external bias for the first time. High-resolution transmission electron microscope (HRTEM) image has confirmed the layer-by-layer structure of the $200 \times 200$ $nm^2$ via-hole devices. The polycrystalline $GeO_x$ material has $Ge^0$ and $Ge^{4+}$ oxidation states, which is confirmed by X-ray photo-electron spectroscopy. An excellent dc endurance of 1000 cycles and long P/E endurance of $>10^6$ cycles with a small P/E pulse width of 100 ns can be achieved under a low operation current of 0.1 µA. The Fowler-Nordheim (F-N) tunneling conduction dominates at high field in HRS and low field regimes are complied with space-charge limited current conduction (SCLC). This structure has enhanced memory performances with good device-to-device switching uniformity, repeatable multi-level cell (MLC) by varying negative voltage with a high resistance ratio of 600, long P/E endurances of $>10^6$ cycles at high $V_{read}$ of −1V, and robust data retention of $>10^5$s at 85 °C after 1000 P/E cycles. The HRTEM images at 'SET' condition of the device (after $10^6$ cycles of P/E) show the thickness increment of $GeO_x$ layer (12.5 nm vs. 10 nm) along with small nanograins of <7 nm in diameter. The $O^{2-}$ ions migration leads to conducting filament formation/rupture through redox reaction in $GeO_x$ material and changes the $Ge^0/Ge^{4+}$ oxidation states. Therefore, this $W/GeO_x/W$ RRAM device has very high potential to become the successor of 3D flash non-volatile memory (NVM) in future. The $GeO_x$ membrane in EIS structure detects a low concentration of 1 nM $H_2O_2$ through oxidation-reduction reaction in $GeO_x$ material. Sarcosine as a prostate cancer biomarker has been also detected with a low concentration of 50 pM, which will be useful to diagnosis cancer patient at early stage in future.

## Results and Discussion

Figure 1a reveals the cross-sectional TEM image with a small via-hole size of $0.2 \times 0.2$ $\mu m^2$. Cross-sectional high-resolution TEM image inside the via-hole region quantifies the thickness of $GeO_x$ switching material (SM) of approximately 10 nm (Fig. 1b). The Fast Fourier Transformation (FFT) images (inset) of marked region explore that the d-spacing value is 3.9 Å, which lies in between the d- spacing values of Ge (3.27 Å)[28] and $GeO_2$ (4.3 Å)[29] nanocrystals. It assures the formation of polycrystalline $GeO_x$ film with a grain size of approximately 10 nm in pristine device. In order to understand the elemental composition and defects in the $GeO_x$ films, the chemical binding states have been investigated by XPS characterization (Fig. 1c,d). Figure 1c shows XPS spectrum of Ge*2p* core-level electrons, which is fitted by using Shirley background subtraction and Gaussian functions. The corresponding binding energies (BE) of the doublet de-convoluted Ge $2p_{3/2}$ spectrum peaks are centered at 1218 and 1220.4 eV. The lower BE peak (1218 eV) is related to the non-oxidized semiconductor Ge ($Ge^0$), while the higher BE peak (1220.4 eV) is assigned to the Ge-O bonding i.e, oxidized $Ge^{4+}$ state[30,31]. Bodlaki *et al*.[30] and Wu *et al*.[31] have reported elemental Ge$2p_{3/2}$ ($Ge^0$ state) peak at 1217.9 and 1217.8 eV, while the $Ge^{4+}$ $2p_{3/2}$ state exists at 1220.6 eV and 1220.1 eV, respectively. The binding energy peaks are very close to our present observation. The estimated ratio of $Ge^0/Ge^{4+}$ peak is approximately1.6. Therefore, the formation of $GeO_x$ ($x \leq 2$) film is confirmed. The O*1s* peak (BE of 530.9 eV) denotes the associated oxygen ions ($O^{2-}$) in $GeO_x$ matrix, as shown in Fig. 1d. Higher BE peak at 531.7 eV addresses to the defects i.e, oxygen deficient ($V_O$) in $GeO_x$ layer. Higher BE peak specifies the presence of large amount $V_O$'s in $GeO_x$ film, as shown in Fig. 1d. In similar way, it is reported that the position of main O*1s* peak which remains bonded with $GeO_x$ at BE of $531.2 \pm 0.2$ eV while the rest one at $532.1 \pm 0.2$ eV indicates the chemisorbed oxygen[32]. In our study, $V_O$'s plays the most important role to originate the formation-free resistive switching via oxidation state changes of $Ge^{4+}/Ge^0$ in $W/GeO_x/W$ structure. Yang *et al*.[33] have also reported the $O^{2-}$ ions migration and oxidation state changes from $Mo^{5+}$ to $Mo^{6+}$ in $Ag/MoO_{3-x}/FTO$ resistive switching memory under external bias. Multi-level resistive switching through $H_2O_2$ sensing mechanism in $W/GeO_x/W$ structure has been discussed later.

Figure 2a shows the formation-free I–V hysteresis characteristics at current compliances of 0.1, 1, 10, and 100 µA. The voltage sweeping directions are indicated by the arrows: $1 \rightarrow 2 \rightarrow 3 \rightarrow 4$. By applying +Ve bias of +3 V on the top electrode (TE), the memory device switches from high resistance state (HRS) to low resistance state (LRS). The SET voltage ($V_{SET}$) is approximately 2.6 V at a low CC of 100 nA. Initially no extra formation voltage process is needed, which is very necessary to reduce power consumption or reduce the process steps in memory circuit. On the other hand, the RRAM device starts to switch back to HRS at the $V_{RESET}/I_{RESET}$ of −0.9 V/8.8 nA. Therefore, this device can be operated with ultra low SET/RESET current of 0.1 µA/8.8 nA at $V_{SET}/V_{RESET}$ of +2.6 V/−0.9 V, which is very important for low energy memory device application. In similar way, the resistive switching occurs at the CCs of 1, 10 and 100 µA having $V_{SET}/V_{RESET}$ of +3.7/−1.3, +4.8/−3 and +4.5/−4.35 V, respectively. All resistance states at each CC can be repeated more than 1000 cycles following the same track (Supplementary Information; Fig. S1). Both HRS and LRS are decreasing with increasing CCs, which can be controlled by controlling CCs. This suggests that the oxidation-reduction occurs at the W TE/$GeO_x$

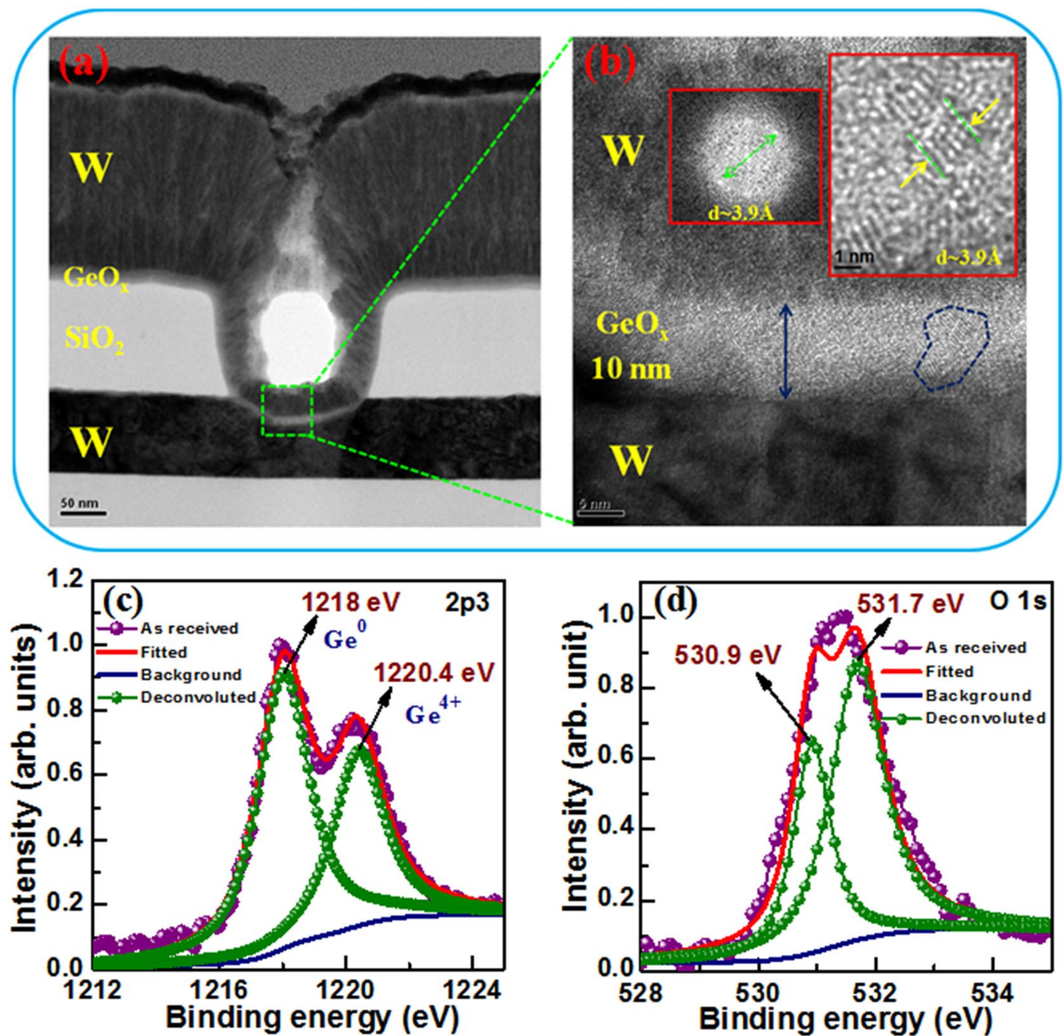


**Figure 1.** (**a**) TEM image of W/$GeO_x$/W memory device having via-hole size of 0.2 × 0.2 μm$^2$. (**b**) HRTEM image exhibits 10 nm-thick polycrystalline $GeO_x$ film and corresponding FFT images (inset) exhibit the d-spacing value. XPS characteristics of (**c**) Ge*2p* and (**d**) O*1s* spectra for the $GeO_x$ films on p-Si substrate.

interface or interface-type[34] resistive switching. The HRS current can be decreased with increasing $V_{STOP}$, which has been explained later. Good switching reliability is one of the challenging issues to implement RRAM for real application. We have analyzed cumulative probability distribution of randomly chosen 50 devices at a CC of 100 μA to confirm the reliability (Fig. 2b). Average values ($\sigma_m$)/standard deviation ($\sigma_s$) for LRS and HRS are found to be 52.5 kΩ/5.7 kΩ and 2.43 MΩ/2.18 MΩ, respectively at a read voltage ($V_{read}$) of 0.2 V. Hence the dispersion ($\sigma_s/\sigma_m$) values are very small of 0.1 and 0.9 for LRS and HRS, respectively. Therefore, the device-to-device switching uniformity yield is good (96%) with higher resistance ratio (HRS/LRS) of approximately 46. To ensure the low current operation reproducibility, Fig. 2c exhibits the resistive switching characteristics of 1000 successive dc switching cycles at 0.1 μA. It is noticed that this structure can produce uniform switching with acceptable resistance ratio of approximately 15 even after 1000 dc cycles, which has been presented also in the Supplementary Information (Fig. S2). In addition, this device shows stable operation with more than $10^6$ P/E cycles under a low P/E current of 100 nA and a small P/E pulse width of 100 ns (Fig. 2d). This implies that the $GeO_x$ SM in a simple W/$GeO_x$/W structure plays a major role to achieve such a low current operation.

To understand the current transport mechanism, double log scale fitting of I-V curves at room temperature in both HRS (Fig. 3a) and LRS (Fig. 3b) is analyzed. There are three regions in HRS current having slope values vary from (i) 0.95 to 1.1 at low bias region then (ii) 1.9 to 2.3 at middle bias region, and finally those values are varied from (iii) 4 to 18.2. On the other side, LRS current consists of two regions having (i) slope values vary from 1 to 1.1 at low bias region and then (ii) 1.7 to 1.8 at higher bias region. Both HRS and LRS currents follow linear relationship, i.e, $I \alpha V$ at low voltage and then quadratic relationship (i.e, $I \alpha V^2$) at high voltage. It signifies that both HRS and LRS currents are Ohmic where thermally generated free electron density becomes much more than the injected electron density from the W electrode. By increasing bias the injected carrier density increases immensely than the thermally generated free carrier density which results current increment rapidly. Thus HRS currents are complied with trap-charge controlled SCLC mechanism. The voltage at which current increases

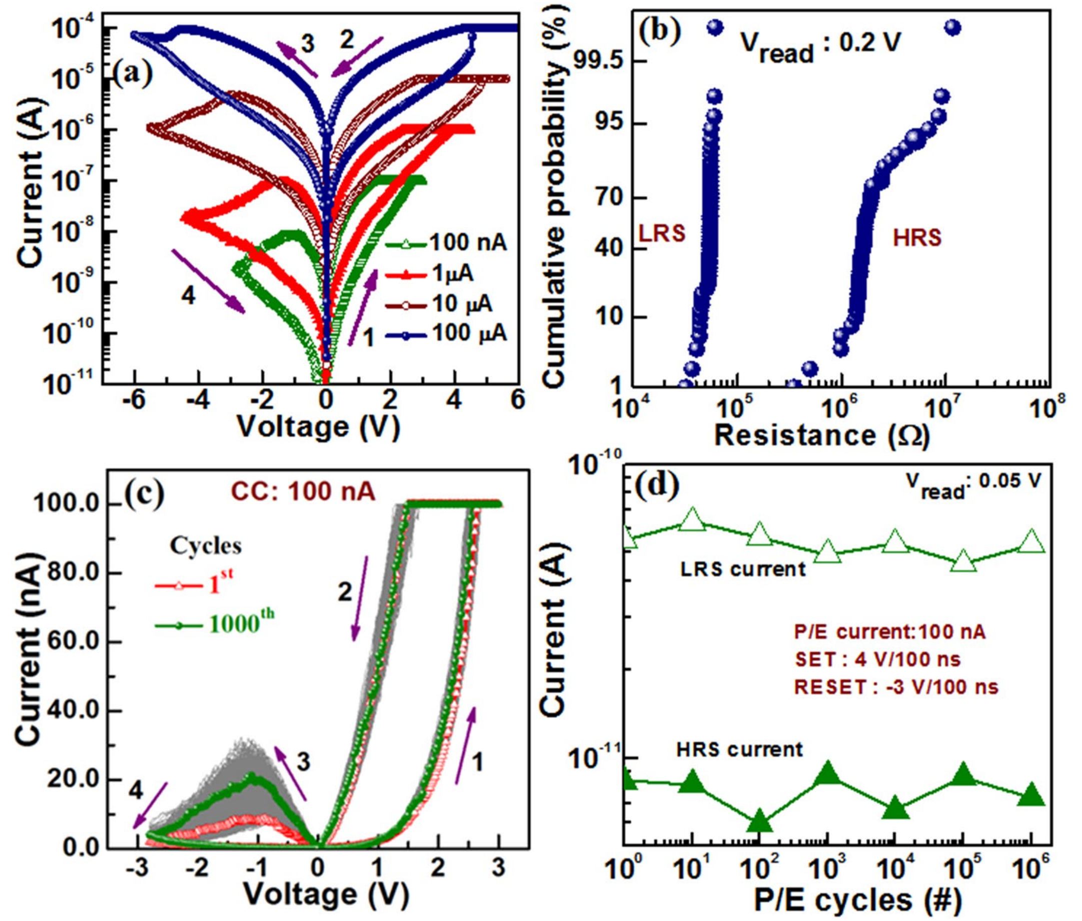


**Figure 2.** (**a**) Bipolar I-V resistive switching characteristics having CCs from 0.1 to 100 μA and (**b**) device-to-device cumulative probability plot at a CC of 100 μA. (**c**) Consecutive > 1000 dc I-V cycles. (**d**) The P/E endurance of >$10^6$ cycles at a low operation current of 100 nA and a small P/E pulse width of 100 ns is applied.

rapidly is reported trap–filled-limited voltage ($V_{TFL}$). Corresponding trap density ($n_t$) has been calculated using the following equation[35],

$$\eta_t = \frac{2\varepsilon\varepsilon_0 V_{TFL}}{qd^2} \tag{1}$$

where $n_t$ is trap density, $q$ is the electronic charge, ε (~12) is the dielectric constant of $GeO_x$, $\varepsilon_0$ is free-space permittivity, $d$ (~10 nm) is the thickness of switching layer. The $V_{TFL}$ values of HRS current at CCs of 0.1, 1, 10 and 100 μA are found to be 1.2, 2.3, 2.9, and 3.3 V, while the $n_t$ values are found to be $1.59 \times 10^{19}$, $3.05 \times 10^{19}$, $3.85 \times 10^{19}$ and $4.4 \times 10^{19}$ $cm^{-3}$, respectively. Similarly, the $V_{TFL}/n_t$ values of 2.48 V/$6.67 \times 10^{16}$ $cm^{-3}$ and 0.46 V/$1.22 \times 10^{16}$ $cm^{-3}$ are reported for FTO/$TiO_2$ and $TiO_2$/$CH_3NH_3PbI_3$/Ag structure, respectively[35]. Higher slope values of HRS current are 9.6 and 18.2 at CC of 10 and 100 μA, respectively, which are owing to F-N tunneling phenomena. Kim *et al*. have reported analogous F-N tunneling phenomena at higher slope value of 6.6 for the HRS currents above $V_{TFL}$ and SCLC mechanism is reported at LRS current in their ITO/GaZnO/ITO structure[36]. To ensure the F-N tunneling conduction, experimental I-V curves of the HRS currents in both + Ve and –Ve bias regions are plotted as ln ($J/E^2$) vs. 1/E (Fig. 3c,d), where $E$ is the electric field. The tunneling barrier heights ($\Phi_b$) have been calculated from the ln ($J/E^2$) vs. 1/E plots using the following F-N tunneling equation below[37],

$$\Phi_b = (-S)^{\frac{2}{3}} \left\{ \frac{\left(\frac{3}{4} q\hbar\right)^2}{2m_{ox}} \right\}^{\frac{2}{3}} \tag{2}$$

where S is the slope, $m_{ox}$ is the tunneling effective mass of electron (or holes) in the $GeO_x$ layer and $\hbar$ is the reduced Planck's constant. The linear fitting nature at CCs of 10 and 100 μA confirms the F-N tunneling conduction above critical electric field ($E_C$) of ≥3 MV/cm[38]. Considering $m_{ox} = 0.2m_0$[39], the calculated values of $\Phi_b$ are 1.14 eV and 0.71 eV at CC of 100 μA for +Ve and -Ve biases, respectively. The $\Phi_b$ values at the TE/$GeO_x$ interface is lower (0.71 eV vs. 1.14 eV) because of more defective than the BE/$GeO_x$ interface. Similarly, the $\Phi_b$ value is

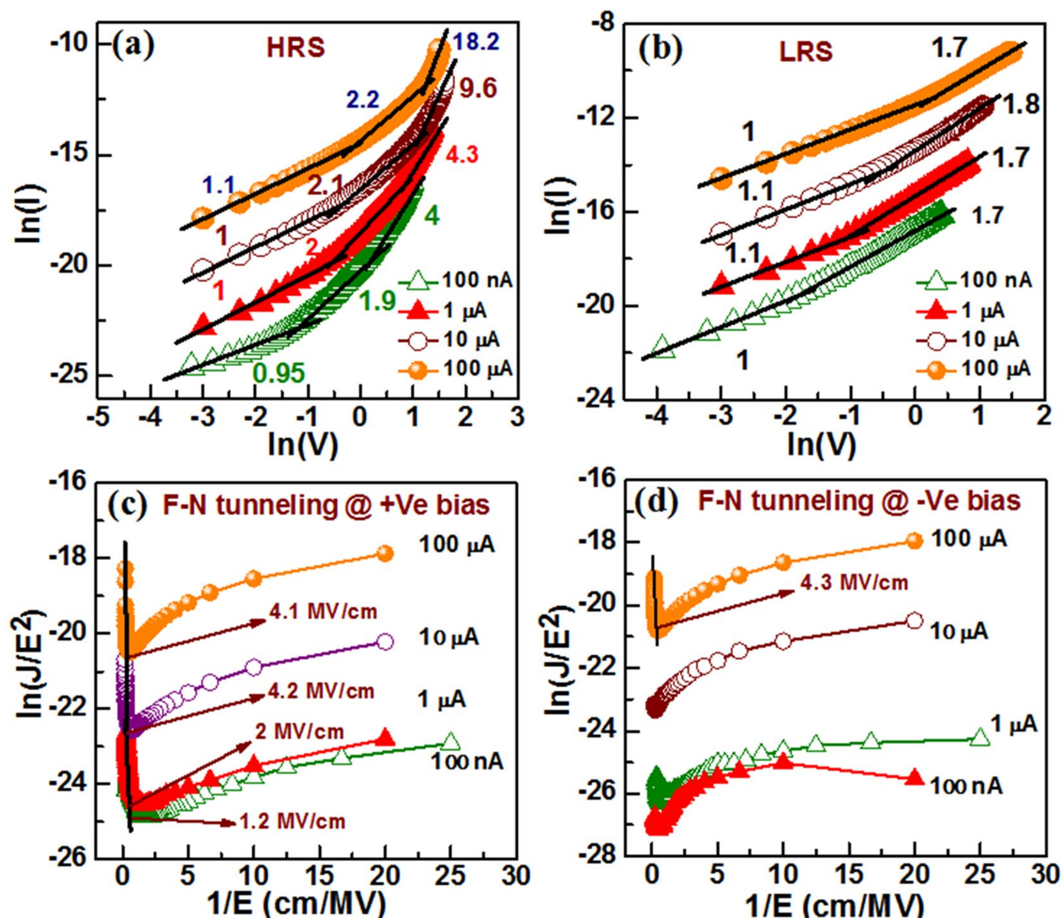


**Figure 3.** Linear fitting of I-V curves in log-log scale at (**a**) HRS and (**b**) LRS current show SCLC nature. F-N tunneling conduction occurs at $E_C > 3$ MV/cm (**c**) in +Ve bias and (**d**) −Ve bias of the HRS currents. The $E_C$ is critical electric field. The F-N tunneling is observed at higher CC of >10 μA.

1.32 eV at +Ve bias for CC of 10 μA. Therefore, electrons tunnel through the triangular potential barrier at W/$GeO_x$ interface into the conduction band of $GeO_x$ film. Since F-N tunneling phenomena have been addressed. On the other hand, the F-N tunneling phenomena are eliminated because of lower bias. Therefore, this is suggested that the HRS current at higher bias of ≥3 V is dominated by F-N tunneling.

Figure 4a shows the typical MLC operation by varying $V_{STOP}$ voltages from −6 to −8V at a CC of 100 μA. The LRS value is independent of the $V_{STOP}$. However, both resistance ratio and $V_{SET}$ increase with increasing the $V_{STOP}$ values (Fig. 4b). This implies that the oxidizing length of the conducting filaments is increased with increasing the $V_{STOP}$ values. The corresponding $\Phi_b$ values also increases from 0.61 eV to 1.12 eV with increasing $V_{STOP}$ value from −6 V to −8V, which is owing to gradual generation of $Ge^{4+}$ ions (explained later). The resistance ratio becomes approximately 600 at a $V_{STOP}$ of −8 V. Stable MLC operation of successive 200 dc cycles at different $V_{STOP}$ values are shown in Fig. 4c. Hseih *et al.*[40] have also executed similar MLC by varying $V_{STOP}$ at higher CC of 1 mA in Ti/MgZnO/Pt structure. Therefore, it can be asserted that the W/$GeO_x$/W structure is worthy of low current multilevel RRAM application under modulation of RESET voltages. From Fig. 4a, the HRS current decreases with increasing $V_{STOP}$ and the device can be operated at approximately 5 μA after $V_{STOP}$ of −8 V. From Fig. 2(a), the HRS currents are not overlapped owing to pristine defects related mechanism at low current operation of <1 μA. As long as the device is operated at higher current (>1 μA), it may not be easy to operate at 100 nA further or highly oxygen reservoir is needed at the W TE/$GeO_x$ interface to re-oxidize the defects. On the other hand, the device should be operated at low current of <1 μA only. However, further study is needed to operate the device at 100 nA by increasing $V_{STOP}$ voltage. This memory device can also perform robust data retention at 85 °C, as shown in Fig. 4d. The data retention is measured after 1000 dc cycles. Both LRS and HRS show long data retention time of $>10^5$ s without any degradation. In order to describe the bipolar resistive switching process, $V_O$ based filamentary-type conduction concept has been established in W/$GeO_x$/W RRAM structure. At first +Ve bias is applied on TE and generated $O^{2-}$ ions are driven towards TE leaving behind the $V_O$'s. These $O^{2-}$ ions are congregated at the TE/$GeO_x$ interface having less possibility of $WO_x$ layer formation because Gibbs free energy of $GeO_2$, $WO_3$ and $WO_2$ are very close to each other say, −518.5, −510 and −506 kJ/mole at 300 K, respectively[11,24,41]. Thus gradually trap density at the TE/$GeO_x$ interface gets lowered and triangular potential barrier is formed which is tunneled by electrons ($e^-$) at the higher electric field. As a result, the TE and BE are connected by $V_O$'s-based filamentary path through which electronic charges flow or the $Ge^0$ based filament is formed under SET operation

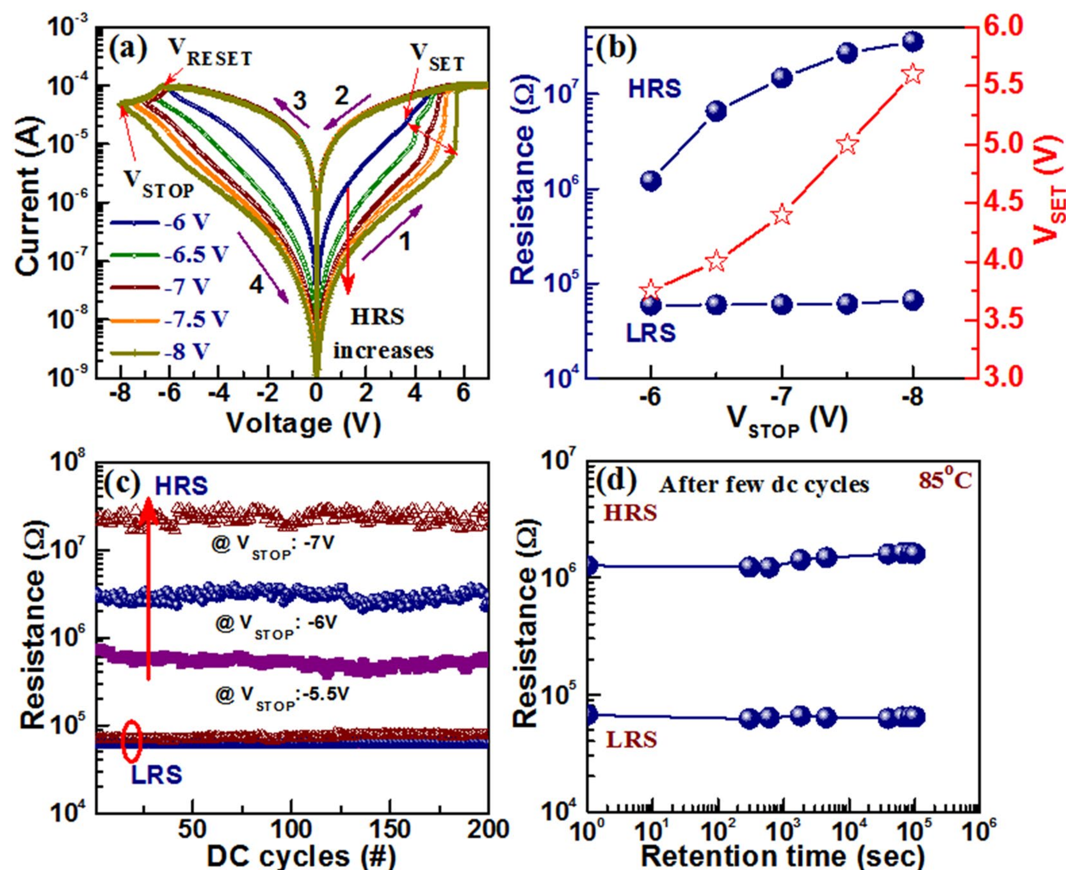


**Figure 4.** (**a**) Influence of $V_{STOP}$'s on HRS currents, (**b**) Both HRS and $V_{SET}$ increases with increasing $V_{STOP}$ values while LRS value is independent. (**c**) MLC operation of HRS with dc cycles by varying $V_{STOP}$ values. (**d**) Long data retention of $>10^5$ sec at 85 °C is obtained after 1000 dc cycles.

and the device turns into LRS. Due to semiconductor in nature of $Ge^0$ (or $Ge^{1+}$, $Ge^{2+}$, $Ge^{3+}$), the SCLC conduction is observed in LRS current (Fig. 3a,b). On the reverse bias, the filament is dissolved by the recombination with repelled $O^{2-}$ ions and a dissolution gap is generated by increasing higher oxidation states or $Ge^0$ to $Ge^{4+}$ states. Eventually device switches back to HRS. Multi-level HRS is observed owing to more generation of $Ge^{4+}$ oxidation states under RESET, which is also explained through $H_2O_2$ sensing later.

To investigate the resistive switching mechanism inside of the polycrystalline $GeO_x$ layer, the TEM images have been taken at 'SET' condition of the memory device after a long P/E endurance of $10^6$ cycles at a high $V_{read}$ of −1V without any series transistor (Fig. 5a). This long endurance is obtained due to our novel $W/GeO_x/W$ structure design. The P/E current, voltage, and pulse width are 100 µA, +6/−6.5 V, and 0.5 ms, respectively. A little variation of HRS is observed than the LRS value because no resistance verification circuit is used. However, the large $V_{read}$ of −1V is used to read during P/E cycles which will be easier for circuit design. There is no report of the switching material and investigation of mechanism after randomly $10^6$ P/E cycles operation, as we have reported in Fig. 5b,c. Basically, a structural change is observed due to combined effect of $O^{2-}$ ions movement and thermal agitation, as shown in Fig. 5c (inset). Isolated small nanograins or nanocrystals (pointed by P1 and P2) with diameters of approximately 2 to 7 nm are observed clearly (density of $2 \times 10^{12}/cm^2$) at 'SET' state. The FFT image (Fig. 5d) and plane spacing image (Fig. 5e) of Ge nanograins show that the d-spacing value is 3.33 Å at the point P1. This is alike to the reported d-spacing values of 3.27 Å and 3.3 Å for Ge nanocrystal in (111) plane[28,42]. Along with that, the d-spacing value of 4.28 Å is obtained from the FFT images (Fig. 5f,g) at the point P2 which indicates the formation of hexagonal $GeO_2$ quartz like nanocrystals at the $TE/GeO_x$ interface. Liu *et al.* have demonstrated the formation of hexagonal quartz like $GeO_2$ nanocrystals with the d-spacing value of 4.3 Å in $(01\bar{1}0)$ plane[29]. Those d-spacing values are quite different as compared to the as-deposited polycrystalline $GeO_x$ SM at pristine state (d = 3.9 Å), as shown in Fig. 1b. Even the grain size is very small after $10^6$ P/E cycles as compared to pristine one (<5 nm vs. 10 nm). This is due to migration of $O^{2-}$ ions under electrical thrust during SET operation towards the $TE/GeO_x$ interface. Consequently, thickness augmentation of the $GeO_x$ layer is also observed (Fig. 5c) at the SET state than the pristine state (~12.5 nm vs. 10 nm). In addition, sufficient localize joule heating factor during random P/E operation also trigger to construct nanograins in the $GeO_x$ layer. Qian *et al.*[43] have shown crystallization from TEM images due to joule heating effect in $ITO/WO_3/ITO$ RRAM structure. To understand the switching mechanism, further study has been explained below.

Figure 6 shows the $H_2O_2$ and sarcosine sensing by using $GeO_x$ membrane in EIS structure. Figure 7 shows measurement set up for $GeO_x$-based sensing membrane in EIS structure. The as-deposited $GeO_x$ membrane shows

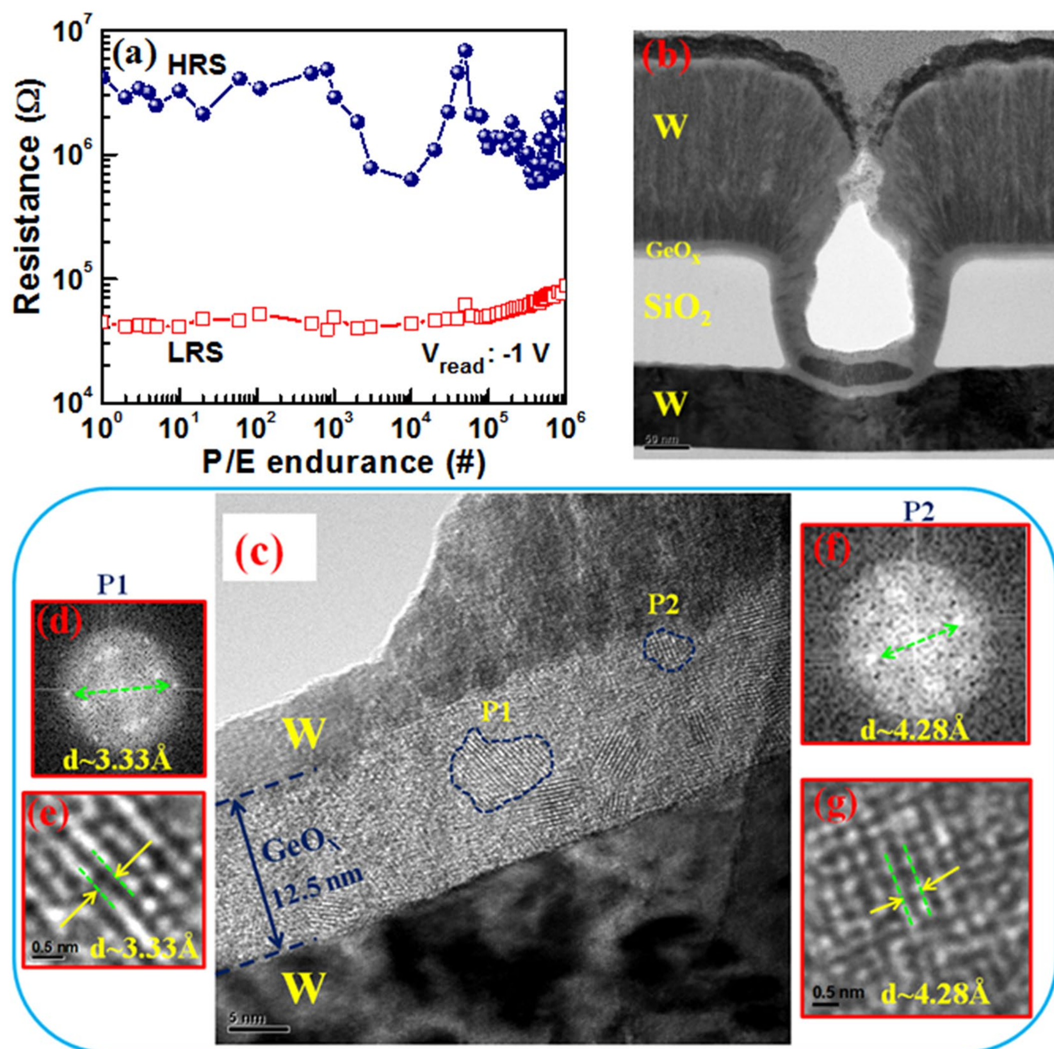


**Figure 5.** (**a**) P/E endurance of >$10^6$ cycles at high $V_{read}$ of −1 V. (**b**) TEM and (**c**) HRTEM images are obtained after P/E endurance of $10^6$ cycles which shows the increment of thickness of $GeO_x$ switching layer than the pristine one (12.5 nm vs. 10 nm). Corresponding FFT images show the formation of (**d,e**) Ge and (**f,g**) $GeO_2$ nanograins or nanocrystals with a small size of 2–7 nm in diameter.

the pH sensitivity of approximately 33 mV/pH with excellent linearity of 99.8% (Supplementary Information; Fig. S3). Adding different pH buffer solutions, the surface charge on membrane is changing. By increasing pH value, the $OH^-$ ions are adsorbed on the sensing surface or reduction of $H^+$ ions. On the other hand, de-protonation[44] occurs on the sensing membrane surface as well as amount of surface potential is reduced. The Si band bending is also decreased as compare to lower pH value. This needs less potential to have a flat-band condition. As a result, the flat-band voltage or reference voltage is shifted towards positive direction. Therefore, the protonation/de-protonation (i.e., $H^+/OH^-$) of the sensing membrane in contact of different pH values changes the reference voltage, which is measured by C-V curves. A similar pH sensitivity of approximately 35 mV/pH is observed for bare $SiO_2$ membrane[45]. In addition, the $H_2O_2$ is an active oxidizing agent which has more application in bio-medical research and will be used here to identify the oxidation states as well as the switching mechanism has been investigated. Figure 6a shows the reference voltage shift with a low concentration of 1 nM $H_2O_2$. The reference voltage shift is approximately 11 mV in presence $H_2O_2$ with PBS (pH 7) solution (inset of Fig. 6a). Our low concentration $H_2O_2$ sensing (1 nM) is comparable with other reported values of 5 nM–3.1 μM by cyclic voltametry measurement[46–50]. Voltage shift occurs due to oxidation of $GeO_x$ membrane using following oxidation-reduction equation below.

$$Ge \leftrightarrow Ge^{2+} + 2e^- \leftrightarrow Ge^{4+} + 4e^- \quad (3)$$

From equation (3), the oxidation state of Ge changes from $Ge^0$ to $Ge^{4+}$ via $Ge^{1+}$, $Ge^{2+}$, $Ge^{3+}$ states[51]. First, $H_2O_2$ in PBS buffer solution will receive electron (e−) from the $GeO_x$ surface (Fig. 7e). This will produce $OH^-$ ions and $OH^*$ radicals in solution ($H_2O_{2+}e^- \leftrightarrow OH^{-+}OH^*$; $OH^* + e^- \leftrightarrow OH^-$). Finally, the $OH^-$ ions will receive $H^+$ ions from the PBS buffer solution and will produce $H_2O$. In this exchange reaction, the pH value of 7 will be

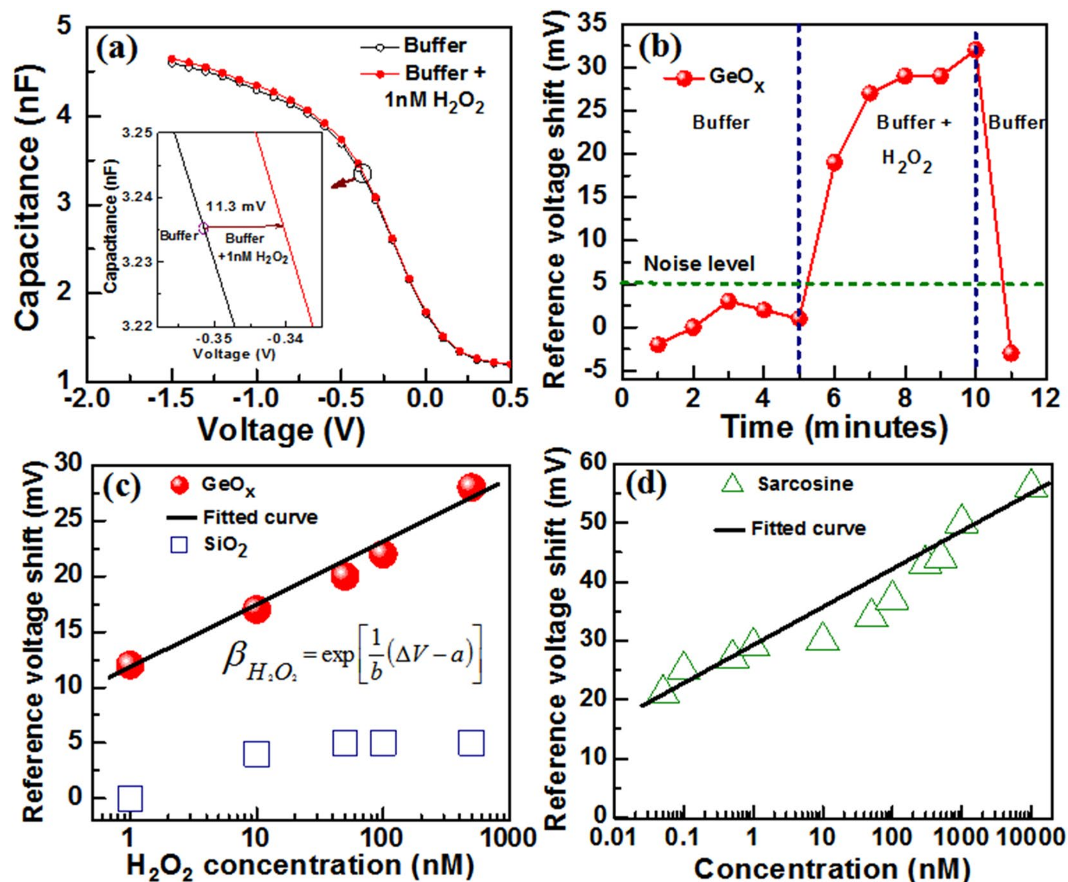


**Figure 6.** (**a**) C-V curve by adding 1 nM $H_2O_2$ in pH7. The reference voltage shift is 11.3 mV, as shown in inset. (**b**) Time-dependent reference voltage shift with and without $H_2O_2$ in PBS buffer solution. This sensor shows reversible phenomena because the $GeO_x$ sensing membrane has redox characteristics. It implies that the sensor can be re-used. This reversible phenomenon makes us understand the resistive switching mechanism through changing $Ge^0/Ge^{4+}$ oxidation states. (**c**) Comparison of $H_2O_2$ detection characteristics between $GeO_x$ and bare $SiO_2$ sensing membranes. The $GeO_x$ membrane can sense $H_2O_2$ with concentration ranging from 1 nM to 500 nM, which is good for real application. (**d**) The reference voltage shift versus sarcosine concentration from 50 pM to 10 µM.

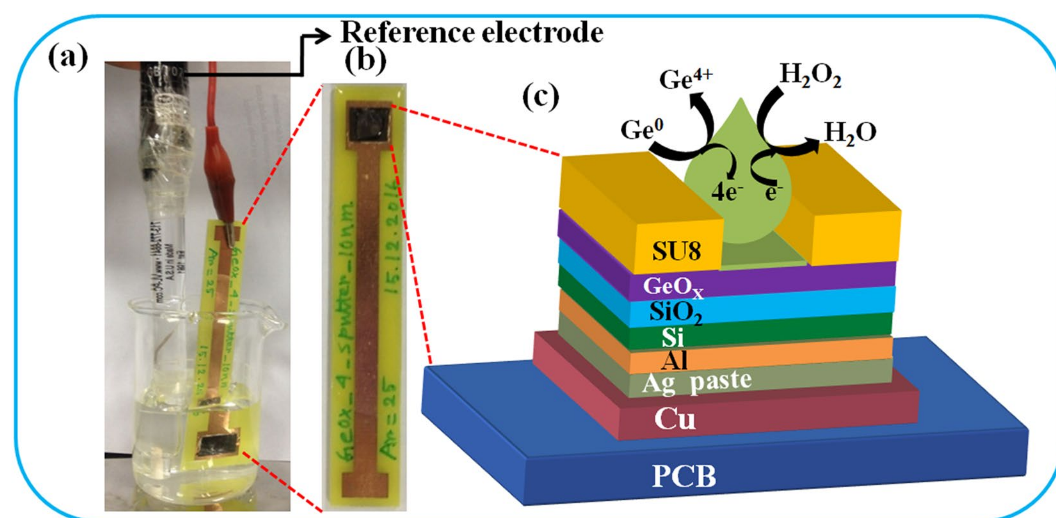


**Figure 7.** (**a**) The sensor chip and Ag/AgCl reference electrode are immersed in PBS buffer solution. (**b**) Sensor chip mounted on PCB and epoxy was used to isolate in between Cu line and sensor. (**c**) Schematic diagram of $GeO_x$-based sensor in electrolyte-insulator-semiconductor structure and oxidation-reduction is shown. This measurement system sets up in our lab.

unchanged. Basically, the $GeO_x$ membrane will be oxidized and the reference voltage will be changed. The work function of Ge is 4.67 eV[52] and it is increased to 4.94 eV[53] for $GeO_2$. By considering the doping ($5 \times 10^{15}\,cm^{-3}$) of p-Si, the work function is 4.94 eV. Therefore, the work function of $GeO_x$ membrane increases with increasing $H_2O_2$ concentration as well as Si band bending is reduced. As a result, the reference voltage is shifted towards positive direction. Previously, we have also reported the oxidation states changed of Zn to ZnO in contact of $H_2O_2$[45]. Figure 6b shows time-dependent $H_2O_2$ response with a concentration of 500 nM. The C-V curve is measured at a regular time interval of 1 minute and the reference voltage is plotted with time. It is clear that the $GeO_x$-based sensor retains to its original response in PBS buffer solution after 5 minutes of $H_2O_2$ sensing. Therefore, this sensor can be used again or the $H_2O_2$ sensing is reversible. Similarly, the resistive switching is also reversible under SET and RESET operation because of redox reaction in $GeO_x$ material. The reference voltage shift gradually increases with successive addition of $H_2O_2$ from 1 nM to 500 nM, where as bare $SiO_2$ based membrane is unable to execute any voltage shift (Fig. 6c). Therefore, the $GeO_x$ membrane has redox properties. We have fitted the reference voltage shift curve of $GeO_x$ sensing membrane and generated mathematical equation is below,

$$\beta_{H_2O_2} = \exp\left[\frac{1}{b}(\Delta V - a)\right] \tag{4}$$

where, $\beta_{H2O2}$ is the concentration of $H_2O_2$, ΔV is the corresponding reference voltage shift, 'b' and 'a' are the slope and intercept of the fitted curve having valued 5.7 and 11.4, respectively. From the above equation (4), a required $H_2O_2$ concentration can be calculated at any arbitrary voltage shift. Figure 6d shows the reference voltage shift with increasing sarcosine concentration from 50 pM to 10 μM. Sarcosine prostate cancer biomarker reacts with enzyme sarcosine oxidase and produces $H_2O_2$ as shown equation (5) below.

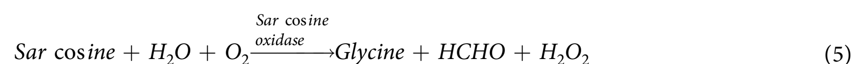

$$Sar\ cosine + H_2O + O_2 \xrightarrow[oxidase]{Sar\ cosine} Glycine + HCHO + H_2O_2 \tag{5}$$

From fitting curve, the values of 'b' and 'a' are found to be 6.1 and 28, respectively. A minimum concentration of 50 pM sarcosine is detected. Both $H_2O_2$ and sarcosine have similar relationship. The pH7 value does not change during successive addition of sarcosine in pBS buffer with enzyme. On the other hand, pure sarcosine with PBS buffer or enzyme with PBS buffer solution does not show reasonable sensing. Therefore, sarcosine concentration (enzyme with PBS buffer solution) will be detected from the reference voltage shift as well as the sensor will be useful to detect early stage of prostate cancer patient in future or prostate cancer can be monitored. Basically, the $H_2O_2$/sarcosine sensing by using $GeO_x$ membrane or switching material proves that the $O^{2-}$ ions migration lead to the oxidation-reduction through changing of $Ge^0/Ge^{4+}$ oxidation states under external bias. This is responsible the switching mechanism and the multi-level occurs owing to more generation of $Ge^0$ under SET or $Ge^{4+}$ under RESET. Therefore, the $GeO_x$ material is not only attractive for multi-level resistive switching memory in a simple W/$GeO_x$/W structure but also could be potentially useful for $H_2O_2$/prostate cancer detection in near future.

## Conclusion

In conclusion, forming-free MLC bipolar resistive switching characteristics and switching mechanism using a simple W/$GeO_x$/W structure, and evidence of redox reaction in $GeO_x$ material through $H_2O_2$ sensing by changing oxidation state of $Ge^0/Ge^{4+}$ have been reported for the first time. The oxidation states are confirmed by XPS. Via-hole device with a size of $200 \times 200\,nm^2$ and polycrystalline grain in $GeO_x$ material are investigated by HRTEM. The W/$GeO_x$/W memory device is able to execute a stable dc endurance of 1000 cycles at ultra low CC of 0.1 μA. The SCLC conduction leads in LRS and low field regime of HRS. But, F-N tunneling dominates in high field regime (>3MV/cm) of HRS. This stack also produces good uniformity, long P/E endurances of $>10^6$ at high $V_{read}$ of −1V, and excellent data retention of $>10^5$ s at 85 °C after few dc cycles at a low operation current of 100 μA. The HRTEM at SET state of the device (after $10^6$ P/E cycles) shows the Ge and $GeO_2$ nanograins with small size of <7 nm as well as the thickness is expanded than the pristine one (12.5 nm vs. 10 nm) due to $O^{2-}$ ions movement and joule heating effect or the conducting filament formation is due to $O^{2-}$ ions migration towards TE/$GeO_x$ interface as well as $Ge^0$ formation through reduction of $GeO_x$. Generation of $Ge^0$ by increasing CC and generation of $Ge^{4+}$ ions (via $Ge^{1+}$, $Ge^{2+}$, $Ge^{3+}$) by increasing $V_{STOP}$ values as well as barrier heights controls the LRS and HRS currents. The redox reaction and understanding of switching mechanism in $GeO_x$ material confirm by measuring $H_2O_2$ sensing with concentration ranging from 1 nM to 500 nM in PBS buffer solution. In addition, sarcosine prostate cancer biomarker with a low concentration of 50 pM is detected successfully. Thus eventually it can be concluded that $GeO_x$-based W/$GeO_x$/W memory device as well as $H_2O_2$/sarcosine sensing will be very propitious for the forthcoming RRAM and bio-sensor for diagnosis of human diseases as well as early detection of prostate cancer in near future.

## Methods

**Memory device fabrication.** Resistive switching memory device with a small via-hole size of $0.2 \times 0.2\,\mu m^2$ was fabricated on 200 nm-thick $SiO_2$ layer. The 8-inch p-type Si wafers were used. A 100 nm-thick W bottom electrode (BE) was deposited by RF magnetron sputtering. To define an active area, a 150 nm-thick $SiO_2$ layer was deposited on the BE. Standard lithography and etching processes were used to expose the active area. Photoresist was used to open active area and the top electrode (TE) regions. Then, a $GeO_x$ switching material (SM) with a thickness of approximately 10 nm was deposited by RF sputtering process by using Ge target (purity: 99.99%) at room temperature. The base pressure of the chamber was $2 \times 10^{-5}$ Torr. Argon (Ar) gas with a flow rate of 25 sccm had been kept fix during deposition and the deposition power was 50 W. The residual oxygen ($O_2$), inside the chamber had been deliberately allowed to react during the deposition of Ge, which created $GeO_x$ layer. Then, a W top electrode (TE) with a thickness of approximately 200 nm was deposited by the same RF sputtering process

using W target (purity: 99.9%). Ar flow rate was 25 sccm and deposition power was 150 W. The deposition time was 30 min. Finally, lift-off process was done to get W/$GeO_x$/W RRAM device with a size of $0.2 \times 0.2\ \mu m^2$. The thickness and microscopic structure of $GeO_x$ layer in W/$GeO_x$/W RRAM device were analyzed by transmission electron microscopy (TEM-JEOL 2100F) with 200 keV energy. Deposition repeatability had been checked by preparing samples three times under invariant conditions along with their electrical measurements. All the electrical characteristics have been measured by Agilent 4156C precision semiconductor analyzer in our lab. Throughout the measurement, sweeping bias is applied on the TE, keeping BE as grounded.

**Sensor fabrication.** A 4-inch p-type Si wafer was cleaned by standard Radio Corporation of America (RCA) process. Then, a 40 nm-thick $SiO_2$ layer was grown on Si by dry oxidation process with a temperature 950 °C in presence of 2.5 sccm $O_2$ gas flow for 70 min. Then, a 10 nm-thick $GeO_x$ film using Ge target was deposited by RF sputtering process. Back side $SiO_2$ layer from the wafers was removed by buffer oxide etchant (BOE) solution. Then, a 300 nm-thick Al back contact was grown by thermal evaporation process. The sensing area of 3.24 $mm^2$ was defined by SU-8 negative photo resist using photo-lithography technique. Finally, the sensor was placed on copper coated printed circuit board (PCB) through Ag paste and it was encapsulated by epoxy to isolate solution from the Si and PCB. Both PCB chip and an Ag/AgCl reference electrode were placed inside a beaker. A 5 ml solution kept in a small glass beaker. To reduce outside noise during capacitance-voltage (C-V) measurement, the glass beaker kept inside black box, which one was purchased from Super Solutions & Services Co., Ltd, Hsinchu, Taiwan. The sensor and reference electrode were connected to HP 4284 A *LCR* semiconductor precision analyzer with computer interfacing. The measurement was controlled the computer and collected all data. The reference electrode and PCB chip are shown in Fig. 7a. The optical microscope image of the PCB chip is shown in Fig. 7b. A schematic view of the sensor in electrolyte-insulator-semiconductor (EIS) structure is shown in Fig. 7c. The oxidation mechanism in contact of $H_2O_2$ solution on $GeO_x$ surface is also demonstrated.

**pH, $H_2O_2$ and sarcosine solution preparation.** In order to check the pH sensitivity and $H_2O_2$ sensing in EIS structure, the pH solutions from 2 to 10 were prepared in the following process. At first, 30 ml of each pH2 to pH10 solution was taken directly into different containers. All the pH solutions were bought from Alfa Aesar Company. Then, the Ag/AgCl reference electrode along with the $GeO_x$ based sensor had been dipped into each solution. The corresponding C-V characteristics were measured at 100 Hz frequency by applying electrode bias in the voltage range from −1.5 volt to 0.5 volt. By calculating the reference voltage shifts at 60% maximum capacitance from pH2 to pH10, the pH sensitivity value was calculated accordingly. For $H_2O_2$ measurement firstly a 1 µM $H_2O_2$ stock was prepared by diluting 10 M $H_2O_2$ concentration with DI water. Later on the PBS (Phosphate Buffer Silane) solution has been prepared by mixing sodium phosphate ($Na_2HPO_4$), sodium diphosphate ($NaH_2PO_4$), sodium chloride (NaCl) and DI water in proper way. The mentioned solutions were purchased from J. T. Baker, Avantor Performance Materials Incorporation. Then, the C-V characteristics are measured by taking 5 ml of 5 mM pH7 PBS solution in a beaker. Then, the reference voltage shifts at 60% of maximum capacitance were measured and the reference voltage versus $H_2O_2$ concentration from 1 nM to 500 nM in PBS solution was plotted.

First, 100 ml of TRIS buffer (purchased from UniRegion Bio-Tech) was diluted in DI water and the pH value was adjusted to pH 7 by monitoring pH meter. Then a stock solution of sarcosine-oxidase with 300 units was diluted in 500 µl TRIS. From the enzyme stock solution, 25 units of enzyme was added in 5 ml of pH7 PBS buffer solution. Sarcosine oxidase was purchased from TOYOBO CO. LTD, Osaka, Japan and sarcosine was purchased from Sigma-Aldrich, China. Now, a 10 mM of sarcosine stock was prepared in DI water. By diluting this stock solution, variation of sarcosine concentration ranging from 50 pM to 10 µM was successively added in the pH7 PBS buffer-enzyme solution and corresponding reference voltage shifts were plotted.

## References


1. Waser, R. & Aono, M. Nanoionics-based resistive switching memories. *Nat. Mater.* **6**, 833–840 (2007).
2. Kumar, S. *et al*. Direct observation of localized radial oxygen migration in functioning tantalum oxide memristors. *Adv. Mater.* **28**, 2772–2776 (2016).
3. Nakamura, H. & Asai, Y. Competitive effects of oxygen vacancy formation and interfacial oxidation on an ultra-thin $HfO_2$-based resistive switching memory: beyond filament and charge hopping models. *Phys. Chem. Chem. Phys.* **18**, 8820–8826 (2016).
4. Zhu, Y. B., Zheng, K., Wu, X. & Ang, L. K. Enhancement stability of filament type resistive switching by interface engineering. *Sci. Rep.* **7**, 43664 (2017).
5. Wang, Q. *et al*. Dynamic moderation of an electric field using a $SiO_2$ switching layer in $TaO_x$-based ReRAM. *Phys. Status Solidi RRL.* **9**, 166–170 (2015).
6. Gao, S. *et al*. Tuning the switching behavior of binary oxide based resistive memory devices by inserting an ultra-thin chemically active metal nanolayer: a case study on the $Ta_2O_5$–Ta system. *Phys. Chem. Chem. Phys.* **17**, 12849–12856 (2015).
7. Yu, S., Chen, H. Y., Gao, B., Kang, J. F. & Wong, H. S. $HfO_x$-based vertical resistive switching random access memory suitable for bit-cost-effective three-dimensional cross-point architecture. *ACS Nano.* **7**, 2320–2325 (2013).
8. Niu, G. *et al*. Material insights of $HfO_2$ based integrated 1-transistor -1-resistor resistive random access memory devices processed by batch atomic layer deposition. *Sci. Rep.* **6**, 28155 (2016).
9. Regoutz, A. *et al*. Role and optimization of the active oxide layer in $TiO_2$ -based RRAM. *Adv. Funct. Mater.* **26**, 507–513 (2016).
10. Wei, J. L. *et al*. Bipolar resistive switching with negative differential resistance effect in a Cu/$BaTiO_3$/Ag device. *Phys. Chem. Chem. Phys.* **19**, 11864–11868 (2017).
11. Cheng, C. H., Chin, A. & Yeh, F. S. Novel ultra-low power RRAM with good endurance and retention. *IEEE VLSI Symp. Tech. Dig.* **978**, 85–86 (2010).
12. Kahan, A., Goodrum, J. W., Singh, R. S. & Mitra, S. S. Polarized reflictivity spectra of tetragonal $GeO_2$. *J. Appl. Phys.* **42**, 4444 (1971).
13. Afanasev, V. V. *et al*. Electronic structure of $GeO_2$-passivated interfaces of (100) Ge with $Al_2O_3$ and $HfO_2$. *Appl. Phys. Lett.* **92**, 022109 (2008).
14. Ghosh, A. *et al*. Growth of Au capped $GeO_2$ nanowires for visible-light photodetection. *Appl. Phys. Lett.* **109**, 123105 (2016).
15. Ray, S. K., Katiyar, K. A. & Raychaudhuri, K. A. One-dimensional Si/Ge nanowires and their heterostructures for multifunctional applications — a review. *Nanotechnology.* **28**, 092001 (2017).

16. Ray, S. K., Maikap, S., Banerjee, W. & Das, S. Nanocrystals for silicon – based light – emitting and memory devices. *J. Phys. D: Appl. Phys.* **46**, 153001 (2013).
17. Zheng, Z. W., Hsu, H. S. & Cheng, C. H. Interface-engineered resistive memory using plasma-modified electrode on polyimide substrate. *Phys. Status Solidi RRL* **8**, 100–104 (2014).
18. Gorshkov, O. N., Antonov, I. N., Belov, A. I., Kasatkin, A. P. & Mikhaylov, A. N. Resistive switching in metal–insulator–metal structures based on germanium oxide and stabilized zirconia. *Tech. Phys. Lett.* **40**, 101–103 (2014).
19. Hu, W., Zou, L., Gao, C., Guo, Y. & Bao, D. High speed and multi-level resistive switching capability of $Ta_2O_5$ thin films for nonvolatile memory application. *J. Alloy. Comp.* **676**, 356–360 (2016).
20. Chen, Y. C., Chung, Y. L., Chen, B. T., Chen, W. C. & Chen, J. S. Revelation on the interrelated mechanism of polarity-dependent and multilevel resistive switching in $TaO_x$-based memory devices. *J. Phys. Chem. C* **117**, 5758–5764 (2013).
21. Li, H. K. *et al*. Study of multilevel high-resistance states in $HfO_x$-based resistive switching random access memory by impedance spectroscopy. *IEEE Trans. Electron Devices* **62**, 2684–2688 (2015).
22. Ye, C. *et al*. Enhanced resistive switching performance for bilayer $HfO_2/TiO_2$ resistive random access memory. *Semicond. Sci. Technol.* **31**, 105005 (2016).
23. Bousoulas, P., Stathopoulos, S., Tsialoukis, D. & Tsoukalas, D. Low-power and highly uniform 3-bit multilevel switching in forming free $TiO_{2-x}$-based RRAM with embedded Pt nanocrystals. *IEEE Electron Device Lett.* **37**, 874–877 (2016).
24. Kim, W., Menzel, S., Wouters, D. J., Waser, R. & Rana, V. 3-Bit multilevel switching by deep reset phenomenon in Pt/W/$TaO_x$/Pt-ReRAM devices. *IEEE Electron Device Lett.* **37**, 564–567 (2016).
25. Sigel, R. L., Miller, K. D. & Jemal, A. Cancer statistic 2015. *CA Canc. J. Clin.* **65**, 5 (2015).
26. Koutros, S. *et al*. Prospective evaluation of serum sarcosine and risk of prostate cancer in the prostate, lung, colorectal and ovarian cancer screening trial. *Carcinogen* **34**, 2281 (2013).
27. Cernei, N. *et al*. Sarcosine as a Potential Prostate Cancer Biomarker—A Review. *Int. J. Mol. Sci.* **14**, 13893–13908 (2013).
28. Bar, R. *et al*. Multilayer Ge nanocrystals embedded within $Al_2O_3$ matrix for high performance floating gate memory devices. *Appl. Phys. Lett.* **107**, 093102 (2015).
29. Liu, P., Wang, C. X., Chen, X. Y. & Yang, G. W. Controllable Fabrication and cathodoluminescence performance of high-index facets $GeO_2$ micro- and nanocubes and spindles upon electrical-field-assisted laser ablation in liquid. *J. Phys. Chem. C* **112**, 13450–13456 (2008).
30. Bodlaki, D., Yamamoto, H., Waldeck, D. H. & Borguet, E. Ambient stability of chemically passivated germanium interfaces. *Surf. Sci.* **543**, 63–74 (2003).
31. Wu, N. *et al*. Effect of surface $NH_3$ anneal on the physical and electrical properties of $HfO_2$ films on Ge substrate. *Appl. Phys. Lett.* **84**, 3741–3743 (2004).
32. Mukherjee, B. *et al*. Direct laser micropatterning of $GeSe_2$ nanostructures film with controlled optoelectrical properties. *RSC Adv.* **4**, 10013–10021 (2014).
33. Yang, C. S. *et al*. Moisture effects on the electrochemical reaction and resistance switching at Ag/molybdenum oxide interfaces. *Phys. Chem. Chem. Phys.* **18**, 12466–12475 (2016).
34. Ielmini, D. & Waser, R. Resistive Switching: From Fundamentals of Nanoionic Redox Processes to Memristive Device Applications. John Wiley & Sons (2016).
35. Yang, D. *et al*. Surface optimization to eliminate hysteresis for record efficiency planar perovskite solar cells. *Energy Environ. Sci.* **9**, 3071 (2016).
36. Kim, A., Song, K., Kim, Y. & Moon, J. All Solution-Processed, Fully Transparent Resistive Memory Devices. *ACS Appl. Mater. Interfaces.* **3**, 4525–4530 (2011).
37. Sze, S. M. Physics of Semiconductor Devices, Hoboken, NJ, USA: Wiley (1981).
38. Mehonic, A. *et al*. Resistive Switching in Silicon Suboxide Films. *J. Appl. Phys.* **111**, 074507 (2012).
39. Shaposhnikov, A. V., Perevalov, T. V., Gritsenko, V. A. & Cheng, C. H., Chin, A. Mechanism of $GeO_2$ resistive switching based on the multi-phonon assisted tunneling between traps. A. *Appl. Phys. Lett.* **100**, 243506 (2012).
40. Hsieh, W. K., Chuang, R. W. & Chang, S. J. Two-bit-per-cell resistive switching memory device with a Ti/MgZnO/Pt structure. *RSC Adv.* **5**, 88166–88170 (2015).
41. Weast (ed.) R. C. CRC Handbook of Chemistry and Physics, 64 ed., CRC Press, Taylor and Francis Group, Newyork (1984).
42. Cho, Y. J. *et al*. Tetragonal Phase Germanium Nanocrystals in Lithium Ion Batteries. *ACS Nano* **7**, 9075–9084 (2013).
43. Qian, K., Cai, G., Nguyen, V. C., Chen, T. & Lee, P. S. Direct observation of conducting filaments in tungsten oxide based transparent resistive switching memory. *ACS Appl. Mater. Interfaces.* **8**, 27885–27891 (2016).
44. Zheng, G., Patolsky, F., Cui, Y., Wang, U. W. & Lieber, M. C. Multiplexed electrical detection of cancer markers with nanowire sensor arrays. *Nat. Biotech* **23**, 1294–1301 (2005).
45. Kumar, P. *et al*. Highly reliable label-free detection of urea/glucose and sensing mechanism using $SiO_2$ and CdSe-ZnS nanoparticles in electrolyte-insulator-semiconductor structure. *J. Electrochem. Soc.* **163**, B580–B587 (2016).
46. Sun, X., Guo, S., Liu, Y. & Sun, S. Dumbbell-like Pt-Pd-$Fe_3O_4$ nanoparticles for enhanced electrochemical detection of $H_2O_2$. *Nano Lett.* **12**, 4859–4863 (2012).
47. Sun, Y. *et al*. Ultra sonic electrodeposition of Pt-Pd alloy nanoparticles on ionic liquid-functionalized graphene paper: towards a flexible and versatile nanohybrid electrode. *Nanoscale* **8**, 1523–1534 (2016).
48. Zhang, Y., Li, Y., Jiang, Y., Li, Y. & Li, S. The synthesis of Au/C/Pt coredouble shell nanocomposite and its application in enzyme-free hydrogen peroxide sensing. *Appl. Surf. Sci.* **378**, 375–383 (2016).
49. Huang, J., Zhu, Y., Zhong, H., Yang, X. & Li, C. Dispersed CuO nanoparticles on a silicon nanowire for improved performance of nonenzymatic $H_2O_2$ detection. *ACS Appl. Mater. Interfaces.* **6**, 7055–7062 (2014).
50. Li, Y., Zhang, J. J., Xuan, J., Jiang, L. P. & Zhu, J. J. Fabrication of a novel nonenzymatic hydrogen peroxide sensor based on Se/Pt nanocomposites. *Electrochem. Commun.* **12**, 777 (2010).
51. Kim, G. S. *et al*. Effective Schottky barrier height lowering of metal/n-Ge with a $TiO_2/GeO_2$ interlayer stack. *ACS Appl. Mater. Interfaces* **8**, 35419–35425 (2016).
52. Hellberg, P. E., Zhang, S. L. & Petersson, C. S. Work function of boron-doped polycrystalline $Si_xGe_{1-x}$ films. *IEEE Electron Device Lett.* **18**, 456–458 (1997).
53. Xu, M. F. *et al*. Aqueous solution-processed $GeO_2$: An anode interfacial layer for high performance and air-stable organic solar cells. *ACS Appl. Mater. Interfaces* **5**, 10866–10873 (2013).

## Acknowledgements

This work was supported by Ministry of Science and Technology (MOST), Taiwan under contract numbers: MOST-104-2221-E-182-075, MOST-105-2221-E-182-002, and Chang Gung Memorial Hospital (CGMH), Linkou under contract number: CMRPD2E0091. The authors are grateful to MSSCORPS CO., LTD., Hsinchu, Taiwan for their TEM analysis. The authors are also grateful to Electronics and Opto-electronics Laboratories (EOL), Industrial Technology Research Institute (ITRI), Hsinchu, Taiwan for their partial experimental support.

## Author Contributions

S.S. wrote the first draft and analyzed data. S.Z.R. fabricated the RRAM device, helped to measured memory characteristics, and modify the manuscript. A.R. fabricated EIS structure and measured C.-V. characteristics. S.J. helped for measurement of the sensors. Both AR and SJ analyzed the sensor characteristics. S.C., R.P., S.R., M.D., and S.G. analyzed memory characteristics. A.P. helped to analyze data and developed software for the memory/sensor measurement set up. S.R. helped also to set up measurement system. H.M.C. and L.N.T. measured XPS of the $GeO_x$ film. They analyzed the spectra. J.T.Q. explained the sensors. S.K.R. helped to explain memory/sensor characteristics and modify the manuscript. This research work was carried out under the instruction of SM. All the authors contributed to the revision of the manuscript. All authors read and approved the final manuscript.

## Additional Information

**Supplementary information** accompanies this paper at doi:10.1038/s41598-017-11657-4

**Competing Interests:** The authors declare that they have no competing interests.

**Publisher's note:** Springer Nature remains neutral with regard to jurisdictional claims in published maps and institutional affiliations.

**Open Access** This article is licensed under a Creative Commons Attribution 4.0 International License, which permits use, sharing, adaptation, distribution and reproduction in any medium or format, as long as you give appropriate credit to the original author(s) and the source, provide a link to the Creative Commons license, and indicate if changes were made. The images or other third party material in this article are included in the article's Creative Commons license, unless indicated otherwise in a credit line to the material. If material is not included in the article's Creative Commons license and your intended use is not permitted by statutory regulation or exceeds the permitted use, you will need to obtain permission directly from the copyright holder. To view a copy of this license, visit http://creativecommons.org/licenses/by/4.0/.

© The Author(s) 2017